Experiments in Fluids 27 (1999) 339–350 © Springer-Verlag 1999

# Underflow of standard sluice gate

**A. Roth, W. H. Hager**



**Abstract** Gate flow is known to be subjected by scale effects. This experimental project adds to the understanding of effects of viscosity and surface tension. Minimum gate openings as a function of channel width are presented for water flow such that the Froude similarity law applies. Also, the upstream extension of the so-called Reynolds ridge is determined.

Further, results are provided to the pressure distributions on the channel bottom and the gate for inviscid flow conditions. The velocity distribution in the gate vicinity is also described. Then, the height and position of shock waves downstream of the gate section are determined. The corner vortices due to stagnation flow are investigated and means of reduction are evaluated. A novel anti-vortex element is described that reduces shock waves to about 50% as compared to untreated gate flow. The device can be simply added to existing gates.

## List of symbols

| | |
|---|---|
| $A$ | relative gate opening |
| $A_n$ | normalized value of $A$ |
| $a$ | gate opening |
| $b$ | channel width |
| $C_c$ | contraction coefficient |
| $C_d$ | discharge coefficient |
| $D_d$ | normalized value of $C_d$ |
| $D_m$ | relative reduced shock wave height |
| $\boldsymbol{F}$ | Froude number |
| $g$ | gravitational acceleration |
| $H$ | stagnation flow depth |
| $H_o$ | approach energy head |
| $H_p$ | relative bottom pressure |
| $H_{pg}$ | normalized gate pressure head |
| $h$ | flow depth |
| $h_o$ | approach flow depth |
| $h_p$ | pressure head |
| $h_{pg}$ | gate pressure head |
| $h_{rm}$ | reduced shock wave height |
| $\Delta H$ | difference of extreme stagnation depths |
| $P_h$ | hydrostatic gate pressure force |
| $Q$ | discharge |
| $R_h$ | hydraulic radius |
| $\boldsymbol{R}$ | Reynolds number |
| $S_f$ | friction slope |
| $T$ | shock wave parameter |
| $U$ | relative streamwise velocity |
| $u$ | streamwise velocity component |
| $X$ | relative streamwise coordinate |
| $X_s$ | relative shock maximum position |
| $x$ | streamwise coordinate |
| $Y$ | normalized transverse coordinate |
| $Y_g$ | normalized transverse coordinate |
| $Y_s$ | relative shock wave height |
| $y$ | transverse coordinate |
| $Z$ | relative position above bed |
| $\bar{Z}$ | relative position above gate crest |
| $z$ | vertical coordinate. |

## Greek Characters

| | |
|---|---|
| $\alpha$ | aspect ratio |
| $\gamma$ | relative gate pressure |
| $\theta$ | shock angle |
| $\lambda$ | relative length of ridge |
| $\Pi$ | force ratio |
| $\nu$ | kinematic viscosity |
| $\rho$ | fluid density |
| $\Phi$ | friction gradient parameter |
| $\sigma$ | surface tension. |

## Subscripts

| | |
|---|---|
| $a$ | based on gate opening |
| $c$ | contracted |
| $E$ | anti-vortex element |
| $g$ | gate |
| $L$ | limit |
| $M$ | maximum |
| $m$ | minimum |
| $o$ | base value |
| $p$ | piezometric |
| $R$ | ridge |
| $s$ | shock wave |
| $u$ | downstream |
| $v$ | vortex |
| $w$ | wall |

*Received*: *27 April 1998*/*Accepted*: *29 September 1998*

A. Roth, W. H. Hager
VAW, ETH-Zentrum, CH-8092 Zurich, Switzerland

*Correspondence to*: W. H. Hager

The first author would like to thank Prof. D. L. Vischer, former Director of VAW, for his steady interest in the research work. The supports of H. Fritz and R. Boes are kindly acknowledged.

Dedicated to Dr. N. Rajaratnam, University of Alberta, a master of experimental hydraulics.

## 1 Introduction

Gates are a hydraulic structure that allow regulation of an upstream water elevation. Among a wide number of gate designs, the so-called standard gate with a vertical gate structure containing a standard crest positioned in an almost horizontal smooth rectangular channel has particular significance in low head applications. Surface roughness of both the channel and the gate is small and thus insignificant. Standard gates are used both in laboratories and in irrigation channels, large sewers or in hydraulic structures.

Compared to overflow structures, or in particular to the sharp-crested weir, standard gates have received scarce attention. The knowledge is particularly poor regarding the basic hydraulics, whereas studies relating to vibration of these gates are available. The present project describes new findings on standard gate flow, involving: (1) Scale effects; (2) Coefficient of discharge; (3) Surface Ridge; (4) Features of shock waves; (5) Velocity field; (6) Bottom and gate pressure distributions; (7) Corner vortices; and (8) Vortex intensities. A novel device to reduce shock waves in the downstream channel is also proposed.

## 2 Present knowledge

The present knowledge on gates was recently summarized by Lewin (1995). There is a short chapter on vertical gates containing some information on discharge and contraction coefficients, with a relatively large scatter of data. This reflects the present state, and gate flow is far from being understood from this point of view, therefore.

Historical studies on underflow gates are available, and it is currently a common belief that the discharge characteristics of vertical gates have been detailed in the past century. This is definitely not the case, because of the accuracy of discharge measurement, and the small hydraulic models often used. Well known approaches include those of Boileau (1848), Bornemann (1871, 1880), containing summaries of the experiments of Lesbros et al. Haberstroh (1890), Gibson (1920), Hurst and Watt (1925), Keutner (1932, 1935), Fawer (1937), Escande (1938), Gentilini (1941), and Smetana (1948). In these historical experimental studies, the exact geometrical configurations are often poorly specified, and the data are not always available. Details of gate fixation are also not described.

The first modern study relating to free gate flow was conducted by Rajaratnam and Subramanya (1967). The coefficient of discharge was related to the difference of flow depths in the up- and downstream sections $h_o - C_c a$, where $h_o$ = approach flow depth, $C_c$ = coefficient of contraction and $a$ = gate opening. According to observations for both free and submerged flow $C_d$ is exclusively a function of the relative gate opening $a/h_o$, and $C_d$ increases slightly as $a/h_o$ increases, starting from $C_d = 0.595$. The effect of skin friction was stated to be the reason for deviations between computations based on the potential flow theory and observations.

Rajaratnam (1977) conducted a second study on vertical gates in a rectangular channel 311 mm wide, with gate openings between 26 and 101 mm. The axial free surface profile downstream of the gate section was shown to be self-similar. Noutsopoulos and Fanariotis (1978) pointed at the significant scatter of data relating to both coefficients of contraction and discharge. The deviations between observations and theory were attributed to the spatial flow characteristics, and the channels too small often used in laboratories.

Nago (1978) made observations in a 400 mm wide rectangular channel with a gate opening of 60 mm. $C_d$ was found to decrease with increasing relative gate opening, from 0.595 for $a/h_o \to 0$ to 0.52 for $a/h_o = 0.50$.

Rajaratnam and Humphries (1982) considered the free flow characteristics upstream of a vertical gate, as an addition to previous studies. The channel used was 311 mm wide, and gate openings were $a = 25$ and 50 mm. Their data refer to the upstream recirculation zone, the bottom pressure distribution, and the velocity field.

Montes (1997) furnished a solution for the 2D outflow using conformal mapping, compared the coefficient of contraction with experiments, and identified deviations due to viscosity effects. The surface profiles up- and downstream from the gate section were studied, exclusively in terms of gate opening. Energy losses across a gate were related to the boundary layer development and the spatial flow features upstream from the gate.

The purpose of this paper is to clarify several points of standard gate flow, including the discharge coefficient, the ridge position, the velocity and pressure distributions, and the shock wave development that was not at all considered up till now. These results may attract and guide numerical modellers of flow. Their results and approaches have not been reviewed here.

## 3 Experiments

The experiments were conducted in a 500 mm wide and 7 m long horizontal and rectangular channel. The width of the approach channel was also reduced to $b = 245$ and 350 mm. The right hand side wall and the channel bottom were coated with PVC, and the left hand side was of glass to allow for visualisation. To improve the approach flow conditions, screens were inserted and surface waves were adequately reduced. The approach flow was thus without flow concentrations, smooth and always in the turbulent smooth regime. The discharge was measured with a V-notch weir located downstream of the channel, to within $\pm 1\%$ or $\pm 0.1\ \mathrm{l\,s^{-1}}$, whichever was larger.

An aluminium gate 499 mm wide, 600 mm high and 10 mm thick was used, of which the crest was of standard geometry, i.e. 2 mm thick with a 45° bevel on the downstream side. The gate could be mounted with variable openings from the channel bottom. No gate slots were provided and water tightness was assured with a conventional tape. Only free gate flow was considered. The gate opening was varied from $a = 10$–120 mm. Prefabricated elements of a specified height ($\pm 0.1$ mm) were slid below the gate, and removed after the gate was positioned. This procedure was found to be accurate compared to the opening measurement of a positioned gate.

Free surface profiles were measured with a point gage of $\pm 0.5$ mm reading accuracy. Due to free surface turbulence, flow depths could be read only to the nearest mm. For the shock waves described below, turbulence effects were larger,

and the reading accuracy was within $\pm 2$ mm. The reading position was determined with a meter along the channel, to within $\pm 5$ mm.

Velocities were measured with a miniature propeller meter of 8 mm internal diameter to within $\pm 5\%$. In addition, particle image velocimetry (PIV) was used to determine the velocity field in the vicinity of the gate section. Pressure heads on the channel bottom and on the standard gate were measured with a manometer, to within $\pm 2$ mm. The diameter of the pressure tappings was 1 mm.

The experimental program aimed at analyzing the effects of scale, the free surface profile, the development of corner eddies, the determination and reduction of shock waves, and the velocity and pressure characteristics in the gate vicinity. These items are discussed in the following.

## 4
## Gate flow characteristics

Figure 1 shows a definition sketch of a standard gate, i.e. a vertical gate with a sharp outflow crest positioned in a horizontal rectangular channel with a small boundary roughness. The main parameters of gate flow are $Q$ = discharge, $h_o$ = approach flow depth, $a$ = gate opening, $x$ = streamwise coordinate measured from the gate section, $z$ = vertical coordinate measured form the channel bottom, $x_R$ = position of ridge (see below), $h_p$ = piezometric head on channel bottom, $x_s$ = position of maximum shock wave height $h_s$, and $h_u$ = axial downstream depth.

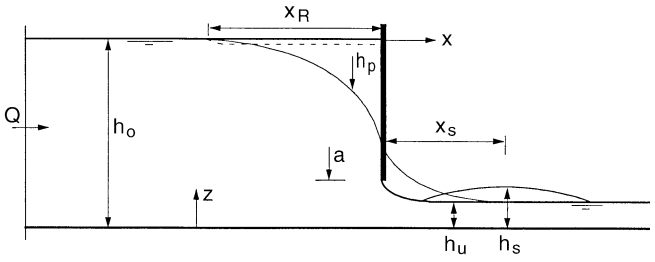


**Fig. 1.** Definition plot of standard gate, with notation



### 4.1
### Discharge coefficient

The discharge under a gate structure can be expressed as

$$Q = C_d ab(2gh_o)^{1/2} \quad (1)$$

with $C_d$ = discharge coefficient. Figure 2a shows $C_d(A)$ where $A = a/h_o$ = relative gate opening. For $a \geqslant 50$ mm, all data follow a single curve, based on the Froude similarity law. For $a < 50$ mm, the curves $C_d(A)$ split, however. For these data,

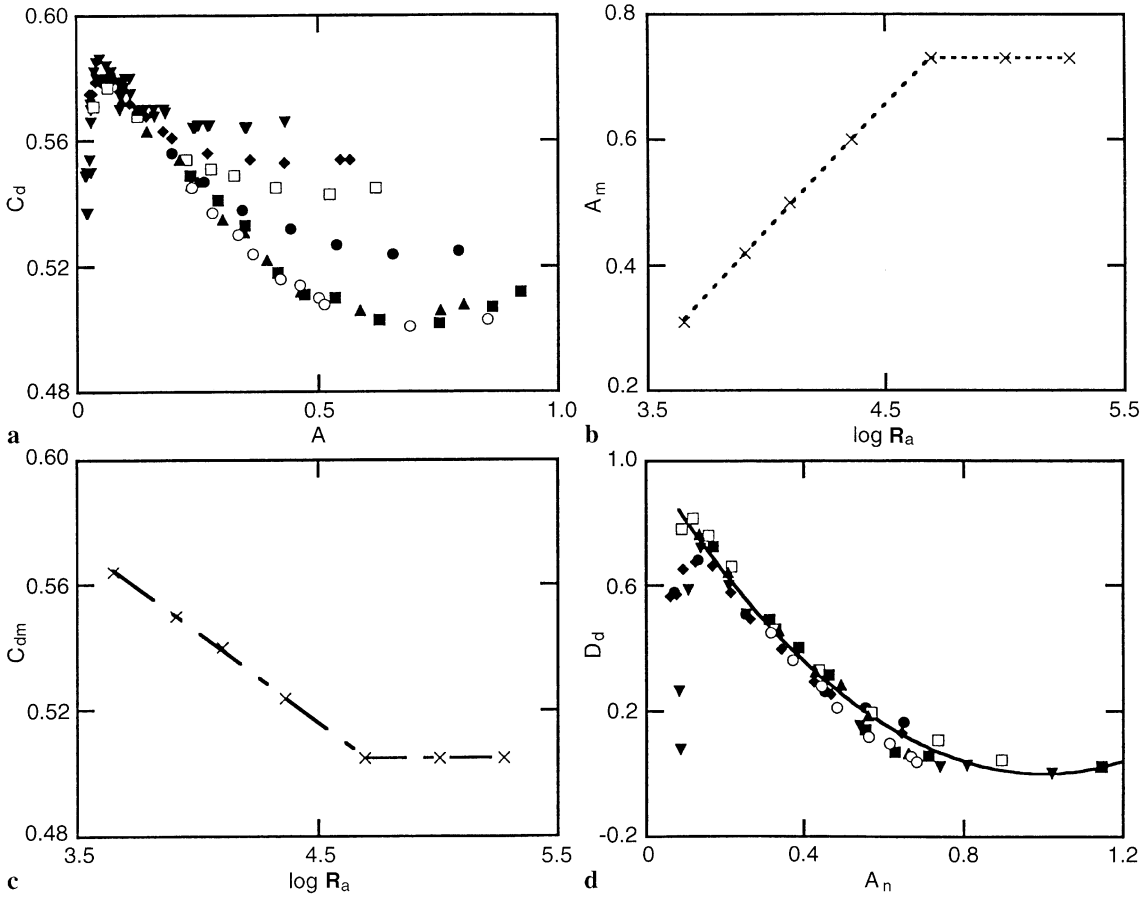


**Fig. 2.** Discharge coefficient **a** $C_d(A)$, **b** minimum value $A_m(R_a)$, (···) Eq. (2), **c** $C_{dm}(R_a)$ (- - -) Eq. (3), **d** relative value $D_d(A_n)$, (—) Eq. (4). $a$(mm) = (▼) 10, (◆) 15, (□) 20, (●) 30, (▲) 50, (■) 80, (○) 120

effects of viscosity are significant, indicating a scale effect. For extremely small values of $A$, surface tension dominates the flow, and $C_d$ decreases sharply to zero. This domain was not further investigated.

All curves $C_d(A)$ start close to 0.60, decrease to a minimum value $C_{dm}$ with the corresponding relative gate opening $A_m$, and increase again. Both $A_m$ and $C_{dm}$ vary essentially with the gate Reynolds number $\boldsymbol{R}_a = a(2ga)^{1/2}\nu^{-1}$. For $\boldsymbol{R}_a < 5 \times 10^4$ the data follow the curves (Figs. 2b and c)

$$A_m = 0.05 + 0.40 \log(\boldsymbol{R}_a/1000) \tag{2}$$



$$C_{dm} = 0.60 - \tfrac{1}{18} \log(\boldsymbol{R}_a/1000) \tag{3}$$

Introducing $D_d = (C_d - C_{dm})/(C_{do} - C_{dm})$ all data for $C_d$ can be expressed as a function of $A_n = A/A_m$, with $C_{do} = 0.594$ as the base value for small A. Figure 2d shows the similarity plot

$$D_d = (1 - A_n)^2 \tag{4}$$

For $b = 500$ mm, the gate opening must be at least $a = 50$ mm for satisfying the Froude similarity law. Equation (4) is a generalisation, including both gravitational and viscous effects.

## 4.2 Effect of channel width

The discharge coefficient was also determined for channel widths $b = 245$ and 350 mm. The limit (subscript $L$) gate openings for Froude similarity to apply are $a_L = 90$, 70 mm, respectively. Accordingly, the channel width has a significant effect on the limit gate opening.

The reason for the scale effect is mainly fluid viscosity (Montes 1997). For these flows, the head losses exceed a certain limit value, due to an extremely small downstream flow depth. To advance a hydraulic approach, the viscosity effect was computed for a simplified flow configuration with a flow depth $h = h_u = C_c a$ along the contraction length $2a$ downstream from the gate.

The friction slope $S_f$ times the contraction length divided by the contracted velocity $u_u = Q/(C_c ab)$ was postulated an index for Reynolds effects. The parameter $\Phi = S_f(2a)/[u_u^2/(2g)]$ is almost a constant for the three limit conditions previously determined. Knowing $\Phi = \Phi_L$ allows prediction of $a_L$ for channel widths smaller and larger than considered experimentally.

For the turbulent smooth regime, the Colebrook–White equation can be approximated as $f = 0.2\boldsymbol{R}^{-0.2}$, where $\boldsymbol{R} = u(4R_h)\nu^{-1}$ with $R_h$ = hydraulic radius. Inserting the parameters gives

$$\Phi = \frac{0.4a}{4R_h \boldsymbol{R}^{0.2}} = \frac{0.4a}{(4R_h)^{1.2}} \left(\frac{\nu C_c}{C_d}\right)^{0.2} (2gh_o)^{-0.1} \tag{5}$$

when expressing discharge $Q$ with Eq. (1). For $a > a_L$, the Bernoulli equation relates $C_d$ and $C_c$ as

$$C_d = C_c(1 + C_c A)^{-1/2} \tag{6}$$

The parameter $\Phi$ may thus be reduced with the aspect ratio $\alpha = a/b$ to

$$\Phi = 0.071\, C_c^{-1.2} \left(\frac{\nu^2}{ga^3}\right)^{0.1} [A(1 + C_c A)]^{0.1} (1 + 2C_c\alpha)^{1.2} \tag{7}$$

It accounts for the gate and channel characteristics, and the Reynolds number based on length $a$.

Inserting in Eq. (7) the limit condition $A \cong 0.25$ yields for all three channel widths the limit value $\Phi_L = 0.02$. Figure 3a shows the predictions for $a_L$ and indicates that the minimum gate opening $a_L$ varies inversely with $b$. For $b > 1$ m, the minimum value tends to $a_L = 45$ mm. It may thus be stated that for any channel width, a minimum gate opening of about 50 mm is required for inviscid flow. For narrower channels, the minimum gate opening increases.

The contraction coefficient $C_c$ was also determined as a function of $A$, and varies slightly for $A < 0.5$ and inviscid flow. A typical value is $C_c = 0.595$. For flows influenced by scale effects, $C_c$ increases with $A$. Detailed results are not presented here for reasons of space limitations.

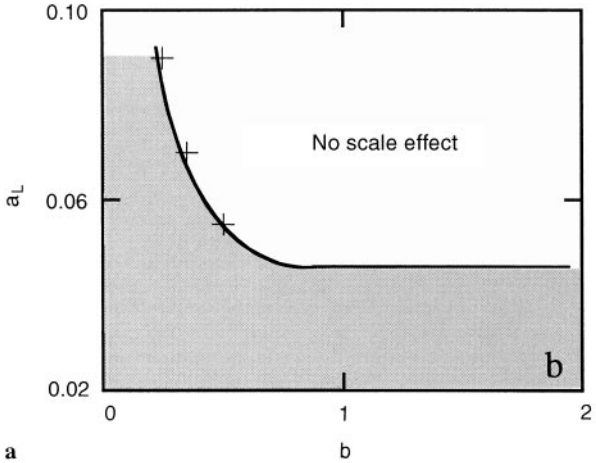


a

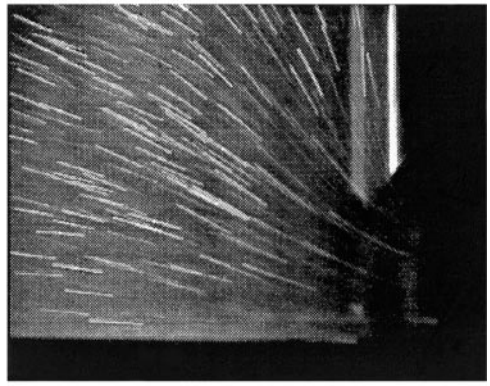

b

**Fig. 3.** **a** Limit gate opening $a_L$(m) as a function of channel width $b$(m) for Froude similarity. (+) observations, (—) Eq. (7). **b** Basis of PIV observations

### 4.3
### Position of ridge

Harber and Gulliver (1992) presented a detailed analysis on the so-called Reynolds ridge visible in front of gates and corresponding to the plunging point of stagnation flow (Fig. 4b). The Reynolds ridge depends on surface tension and was also determined by Rajaratnam and Humphries (1982). It is a significant feature related to water quality because floating matter is retained from the downflow, except for entrainment by corner vortices.

For common laboratory water, one may assume a surface tension height $[\sigma/(\rho g)]^{1/2} = 2.7 \times 10^{-3}$ m, with $\sigma$ = surface tension, and $\rho$ = fluid density. The relative position of ridge $\lambda = x_R/[\sigma/(\rho g)]$ upstream from the gate (Fig. 1) varies inversely with the relative gate opening. Our data are shown in Fig. 4a, together with those of Rajaratnam and Humphries (1982) that are influenced by viscosity, and $\lambda^{-1}$ is somewhat smaller than for our data, which may be approximated as

$$\lambda^{-1} = 0.04A \tag{8}$$

The ridge position thus increases as the relative gate opening decreases.

### 4.4
### Shockwaves

Shocks downstream of a gate are essentially due to corner vortices and may be characterized by the maximum wave height $h_s$, the corresponding location $x_s$ and the shock angle $\theta$ (Fig. 1). Their features are influenced by the contracted Froude number $F_c = Q/[bh_u(2gh_u)^{1/2}] = 2^{1/2}C_d/(C_c^{3/2}A^{1/2})$. For inviscid gate flow $C_d$ and $C_c$ are nearly equal, and the governing parameter for shock waves is $T = (2/A)^{1/2} - 1$. Figure 5 relates to the relative height $Y_s = h_s/h_u$, the relative position $X_s = x_s/h_u$ and the shock angle $\theta$. For inviscid gate flow, the following relations hold

$$Y_s = 0.30T^{2/3} \tag{9}$$

$$X_s = 2T \tag{10}$$

$$\cot\theta = (20/3)T \tag{11}$$

Additional observations for both relative height and position were collected in a bottom outlet 300 mm wide. The pressure head upstream from the gate could be increased up to 25 m. The resulting shocks were all aerated and $Y_s$ was larger compared to the observations in the 500 mm wide channel with the free surface approach flow. Also, the position of maximum wave height was significantly closer to the gate because of the different approach flow geometry. The data for the shock angle are not shown here.

### 4.5
### Velocity distribution

Figure 6a shows the axial horizontal velocity component $u$ for a gate opening $a = 80$ mm. The normalizing velocity $(2gh_o)^{1/2}$ refers to downstream conditions, where the velocities are properly scaled. Upstream from the gate the velocity scale would be $Q/(bh_o)$. For both $X < -2$ and $X > +2$, the velocity distribution is almost uniform, except for the bottom boundary layer. Close to the gate section, the velocity increases significantly with the depth $Z$. Here, $X = x/a$ and $Z = z/a$. Figure 6b is based on video observations in which 0.2 mm VESTIRON particles were illuminated with a light sheet. Such plots are used for further analysis of the internal gate flow features.

### 4.6
### Bottom pressure distribution

The bottom pressure head $h_p(x)$ varies along the channel, from $h_p = h_o$ upstream from the gate section to $h_p = h_u$ sufficiently downstream from the gate section Fig. 7a refers to the axial bottom pressure head $H_p = (h_p - h_u)/(h_o - h_u)$ as a function of dimensionless location $X = x/a$. All data refer to inviscid flow configurations and the function $H_p(X)$ may be approximated with a Gaussian as

$$H_p = 1 - \exp[-(1/3)(X - 1.7)^2] \tag{12}$$

The reproduction of data is improved as compared with Montes (1997), because flows with a scale effect were excluded. Note that $H_p(0) = 0.618$ is close to the critical depth of open

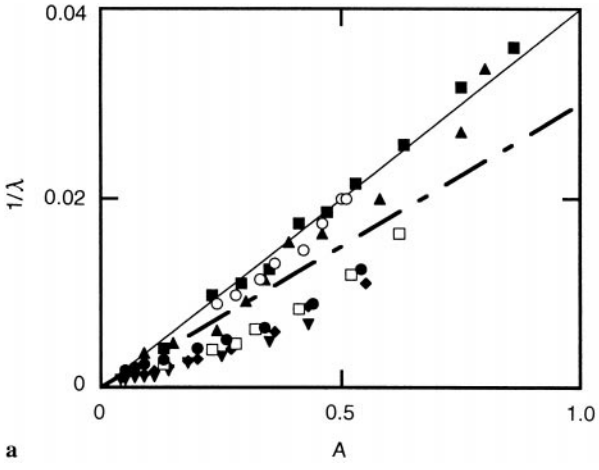


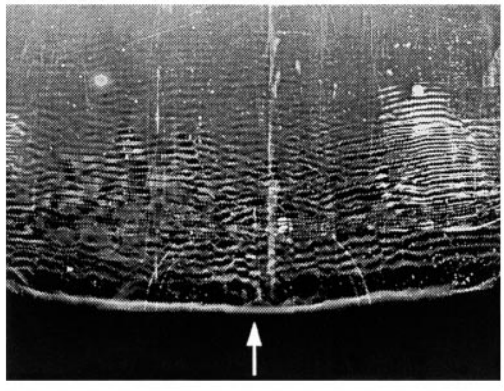


**Fig. 4.** **a** Inverse relative ridge position $\lambda^{-1}$ as a function of $A$; (- . -) Rajaratnam and Humphries (1982) for viscous flow, (—) Eq. (8), notation Fig. 2. **b** Reynolds ridge upstream of gate

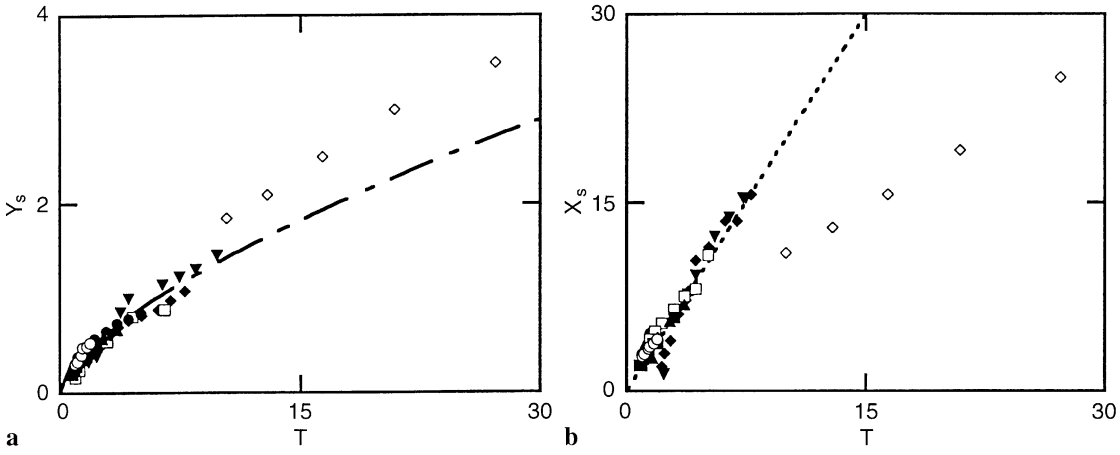


**Fig. 5.** Shock waves downstream of gate **a** $Y_s(T)$ with (- . -) Eq. (9). **b** $X_s(T)$ with ( … ) Eq. (10). Notation Fig. 1, (◇) bottom outlet data

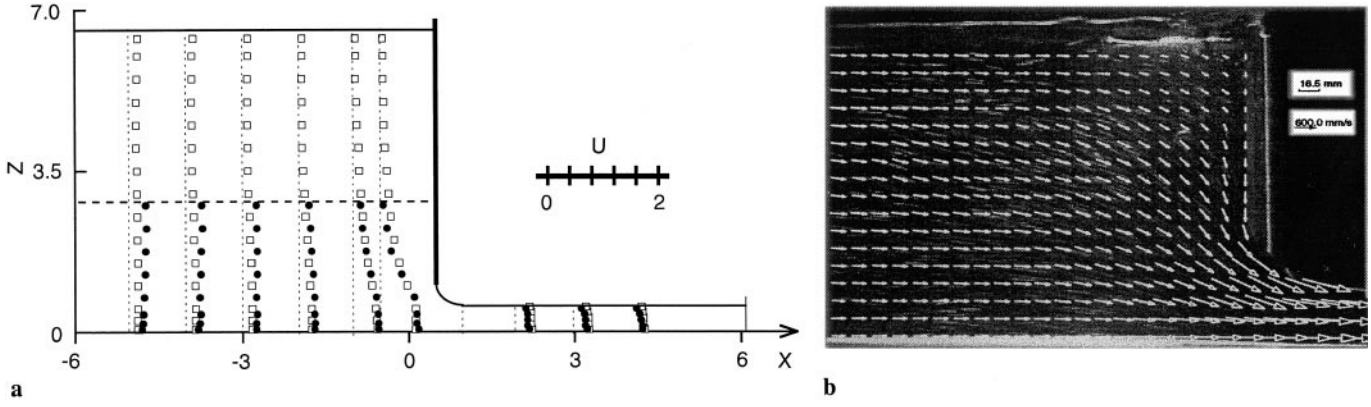


**Fig. 6.** **a** Axial streamwise velocity components $U(X, Z)$ for $h_o$(mm) = (●) 235, (□) 530, **b** velocity vector field for $h_o = 300$ mm. $a = 80$ mm, $b = 500$ mm

channel flow. The transition from the subcritical upstream flow to the supercritical downstream gate flow is thus forced by the presence of the gate. Note also the steep pressure head gradient close to $X = 0$. Figure 7b shows underflow of a standard gate, with a typical stagnation vortex at the upstream surface. The effect of non-hydrostatic pressure is confined to $-2 < X < +2$, as for the velocity field.

### 4.7 Gate pressure distribution

The pressure head on the gate $h_{pg}$ was measured both axially and 50 mm away from the side wall. The axial flow depth at the gate was equal to the stagnation water depth $H_o$, i.e. the energy head of the approach flow $H_o = h_o + Q^2/(2gb^2h_o^2) = h_o(1 + C_d^2A^2)$ from Eq. (1). Figure 8a shows the normalized gate pressure distribution $H_{pg} = h_{pg}/(H_o - a)$ as a function of dimensionless depth $\bar{Z} = (z - a)/(H_o - a)$. A maximum (subscript $M$) pressure head $H_{pgM}$ can be identified, which varies for inviscid flow exclusively with $A$ as (Fig. 8b)

$$1 - H_{pgM} = 0.30 \tanh(2.3A^{0.5}) \quad (13)$$

The position of maximum pressure head above the channel bottom varies slightly. The plot $\gamma = H_{pg}/H_{pgM}$ against $\bar{Z}$ may be described with the boundary layer type equation (Fig. 8c)

$$\gamma = 1.538(1 - \bar{Z})\bar{Z}^{1/7} \quad (14)$$

The pressure distribution is almost hydrostatic close to $\bar{Z} = 1$, and the maximum pressure head is $\gamma_M = 1$ for $\bar{Z} = 1/8$ according to Eq. (14). The gate pressure distribution close to the channel wall follows the axial pressure data, except that they are by 1–2% smaller than the axial data, depending on the approach conditions.

The pressure force on the standard gate can be determined by integration of pressure head over the height $(H_o - a)$. For small gate openings, the result is not exact because of the simplification introduced in Eq. (14). For $A \to 0$, the pressure force is equal to the hydrostatic pressure force $P_h = (1/2)\,b(H_o - a)^2$. The ratio $\Pi$ of effective to hydrostatic pressure forces varies exclusively with $A$, provided viscous flows are excluded. From Fig. 8d, it may be expressed as

$$\Pi = 0.75 + 0.25 \exp(-2.15A^{1.15}) \quad (15)$$

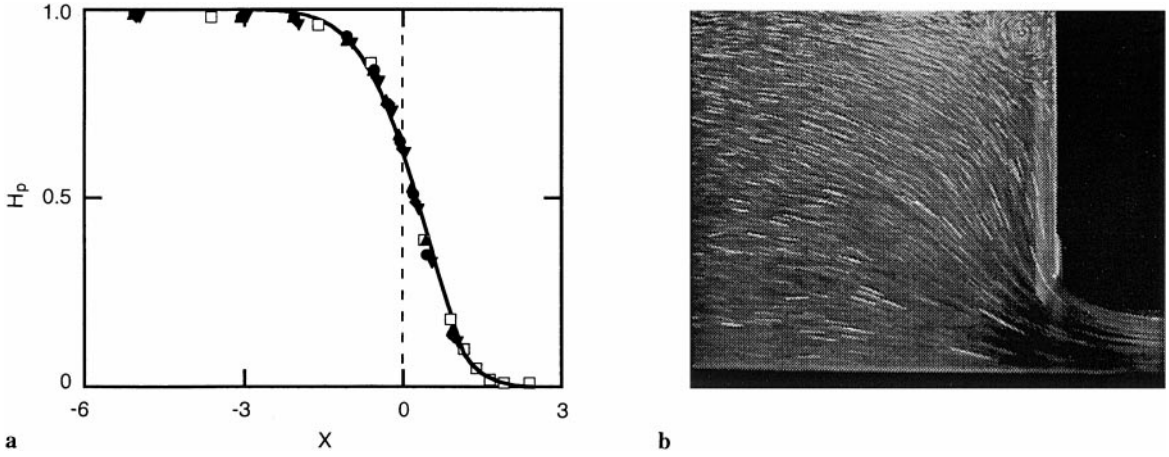


**Fig. 7.** **a** Axial pressure head $H_p(X)$ for $h_o$(mm) = (▼) 234, (◆) 280, (□) 391, (●) 531, and $a = 80$ mm, $b = 500$ mm, (—) Eq. (12), **b** approach flow to standard gate with stagnation vortex

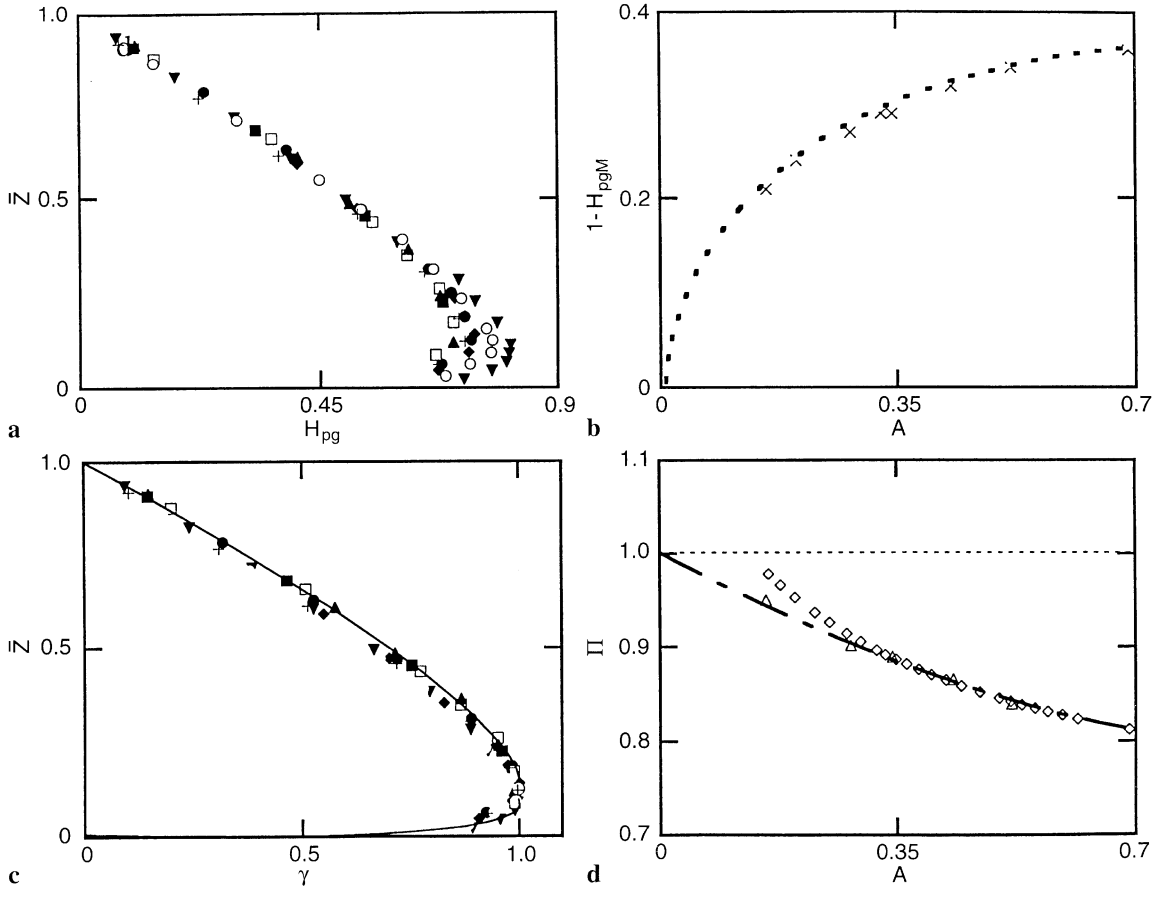


**Fig. 8.** Axial pressure on gate **a** $H_{pg}(\bar{Z})$, **b** $H_{pgM}(A)$ with (×) minimum values observed, (…) Eq. (13), **c** normalized pressure distribution $\gamma$ ($\bar{Z}$), (—) Eq. (14), **d** $\Pi(A)$ with (△) computation (◇) prediction, (—) Eq. (15). $a = 80$ mm, $b = 500$ mm and $h_0$(mm) = (■) 116, (▲) 154, (□) 186, (●) 233, (+) 239, (◆) 283, (○) 396, (▼) 514

The usual simplification $\Pi = 1$ is correct for small $A$, with the dynamic effect significant as $A > 0.10$. For large gate openings, $\Pi$ decreases to about $\Pi = 0.80$, i.e. 20% less than conventionally assumed.

With $\Pi$ given form Eq. (15) one may apply the momentum equation and predict the coefficient of contraction $C_c$, and the coefficient of discharge, using Eq. (6). The analysis is not performed here, but the predictions compare well ($\pm$ 2%)

with observations presented. This check specifies the experimental accuracy, and confirms the domain of flows without scale effects.

## 5
## Corner vortices

Gate flow is characterized by the appearance of two surface vortices located in the corners upstream of the gate. These corner vortices are generated due to the change of direction caused by gate underflow. It can be experimentally demonstrated that these corner vorticities are the origin of the downstream shock waves, and that the shock waves may be reduced by decreasing the intensity of the corner vortices. The following refers to the characteristics of corner vortices first, and then to their reduction by appropriate anti-vortex elements.



### 5.1
### Transverse upstream profile

Corner vortices develop a spatial flow pattern even for an almost 2D approach flow to the gates. *A* characteristic of the spatial flow feature is the transverse profile upstream of the gate, i.e. the stagnation surface profile $H(y_g)$ with $y_g$ = transverse coordinate measured from the channel axis. Let $H_o$ and $H_w$ be the stagnation depths in the channel axis (subscript *o*) and close to the wall (subscript *w*). The dimensionless profile $H_g(Y_g)$ at the gate (subscript *g*) with $H_g=(H-H_w)/(H_o-H_w)$ and $Y_g=y_g/(b/2)$ varies as shown in Fig. 9a. The data scatter because of the turbulent flow and the small differences between $H_o$ and $H_w$ of some mm. An approximation to $\pm 10\%$ is

$$H_g=\exp(-7Y_g^3) \tag{16}$$

The temporally averaged transverse profile has axial maximum and minimum close to the walls. The difference of the extremes $\Delta H=(H_o-H_w)/H_o$ increases essentially with *A* [in rad] as (Fig. 9b)

$$\Delta H=0.0175\ [1-(\cos 2.4A)^2] \tag{17}$$

A maximum value is close to 2%. Such a small difference of heads is able to develop large intake vortices, due to the stagnation flow pattern.

### 5.2
### Corner vortex characteristics

Figure 10 shows a definition sketch of the standard gate with edge vortices. The distance of the vortex (subscript *v*) center from the gate is $x_v$, and the distance from the wall $y_v$. Observations were conducted with channel widths $b=245$, 350 and 500 mm, always for inviscid flow. With $X_v=x_v/a$ and $Y_v=y_v/a$ as non-dimensional parameters, the observations can be expressed as (Fig. 11)

$$X_v=\tfrac{1}{2}A^{-0.75} \tag{18}$$

$$Y_v=\tfrac{2}{3}\exp(-3\alpha) \tag{19}$$

where $\alpha=a/b$ is the aspect ratio at the gate section. The streamwise distance of the vortex center thus increases as

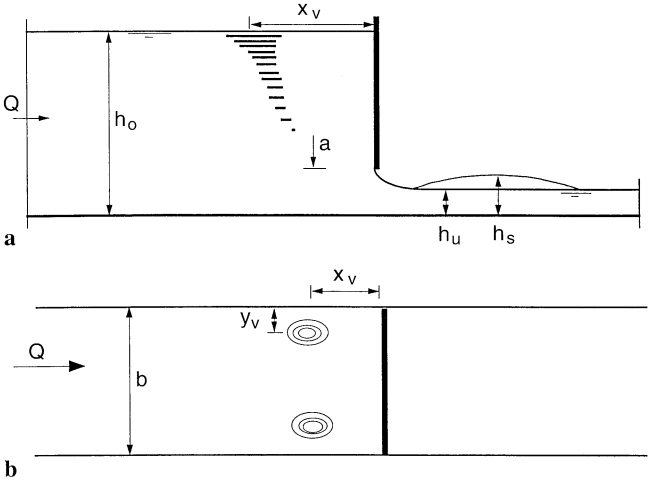


**Fig. 10.** Definition sketch for corner vortices *a* section, **b** plan

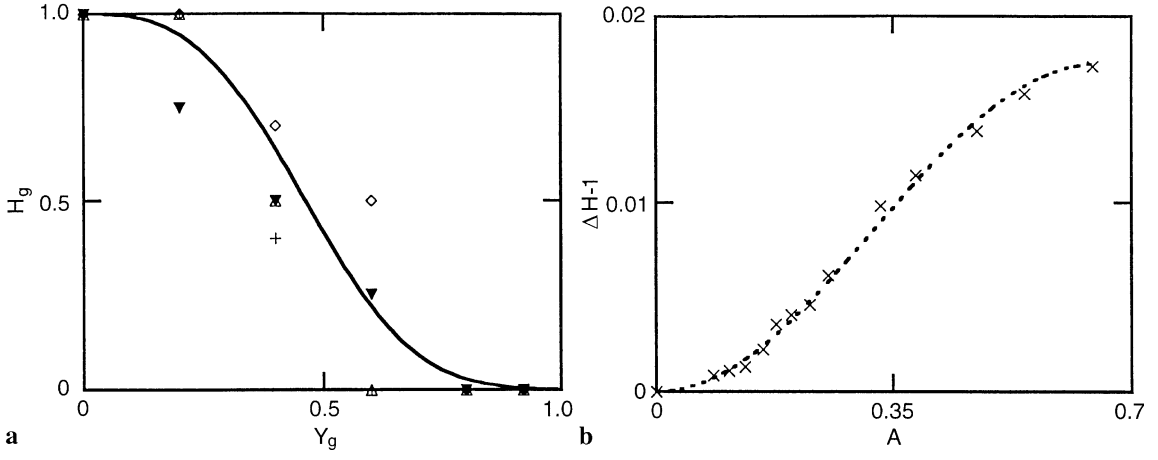


**Fig. 9.** **a** $H_g(Y_g)$ for $h_o$(mm) = (▼) 156, (◇) 218, (△) 280, (+) 379, (—) Eq. (16); **b** $\Delta H(A)$ with (×) observations and (…) Eq. (17) for $a=50$ mm and 80 mm, $b=500$ mm

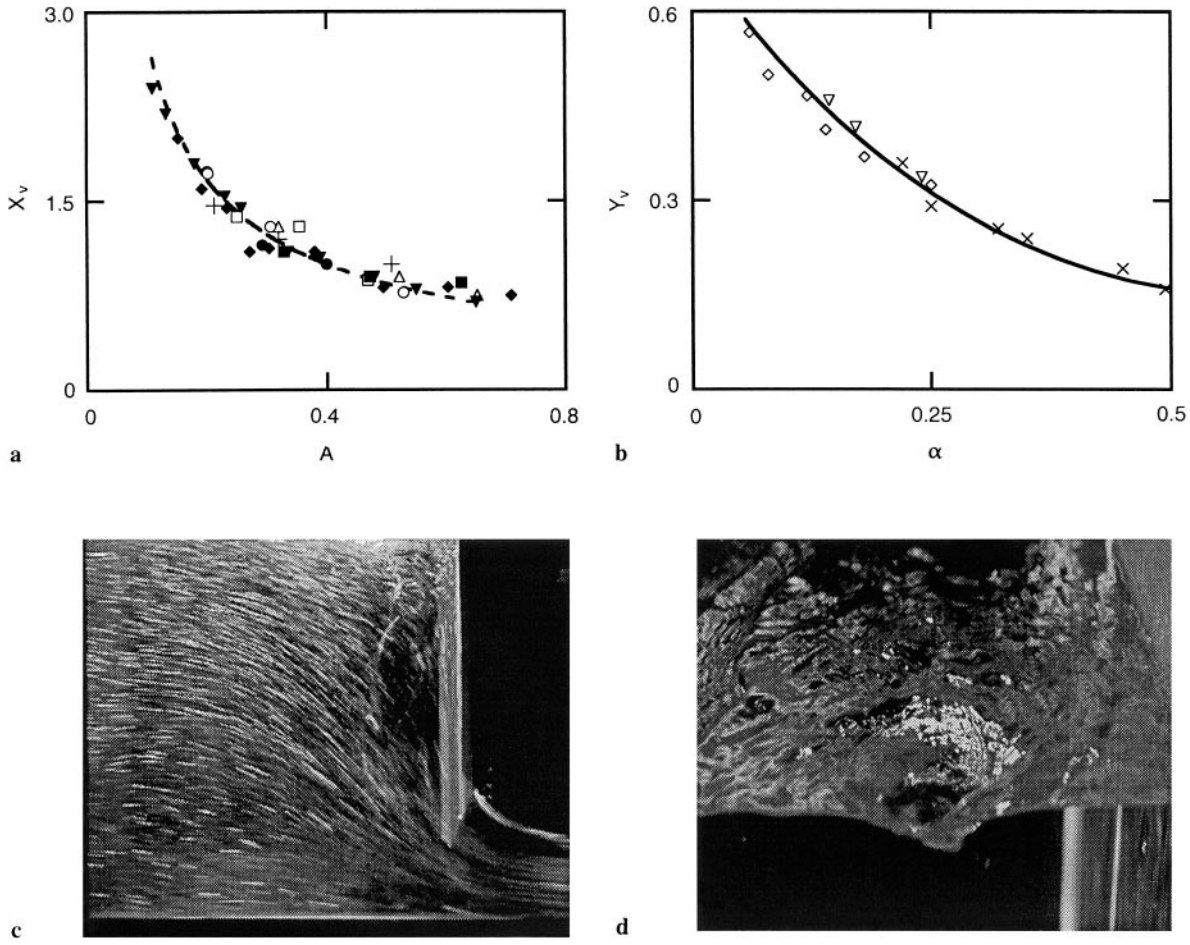


**Fig. 11.** **a** Vortex location $X_v(A)$ for $b = 500$ mm and $a$(mm) = (▼) 50, (●) 80; $b = 350$ mm and $a$ (mm) = (○) 60, (+) 80; $b = 245$ mm, $a$ (mm) = (△) 80, (□) 100, (◆) 120, (…) Eq. (18); **b** vortex distance from wall $Y_v(\alpha)$, for $b$(mm) = (×) 245, (▽) 350, (◇) 500, (—) Eq. (19), **c** vortex flow, **d** surface vortex

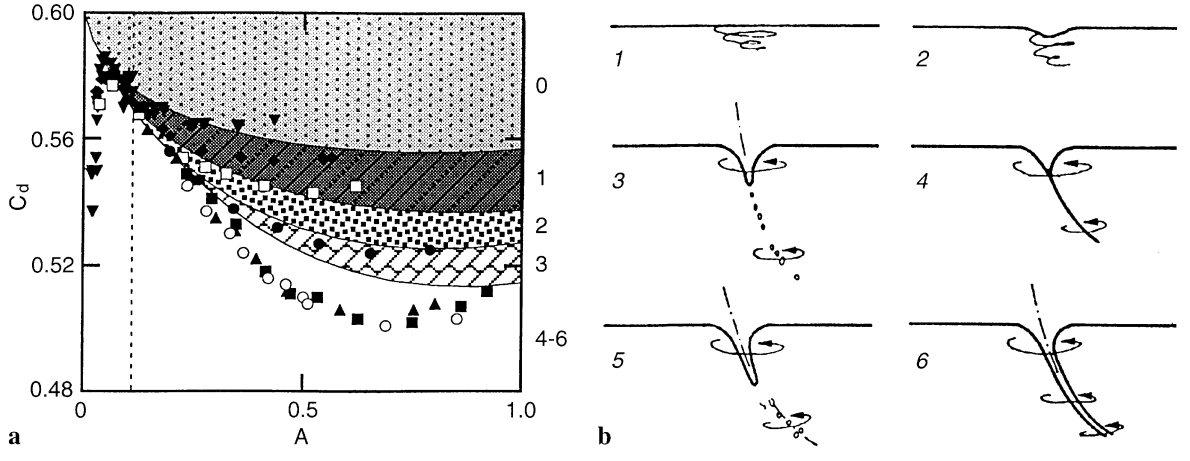


**Fig. 12.** **a** Vortex intensities for standard gate flow and $b = 500$ mm, notation Fig. 2, **b** definition of vortex intensity according to Hecker (1984). *1* Incoherent surface swirl, *2* surface dimple, *3* coherent swirl throughout water column, *4* vortex pulling floating trash, *5* vortex pulling air bubbles, *6* full air core vortex

the relative gate opening decreases, mainly due to the increased distance from the upstream surface to the outlet section. Also, the vortex is closer to the wall for a wide channel than for a narrow channel. Figure 11c relates to the flow pattern with a corner vortex, and Fig. 11d shows a surface vortex of intensity 4 (see below), with the Reynolds ridge on the left side and the gate at the right side.

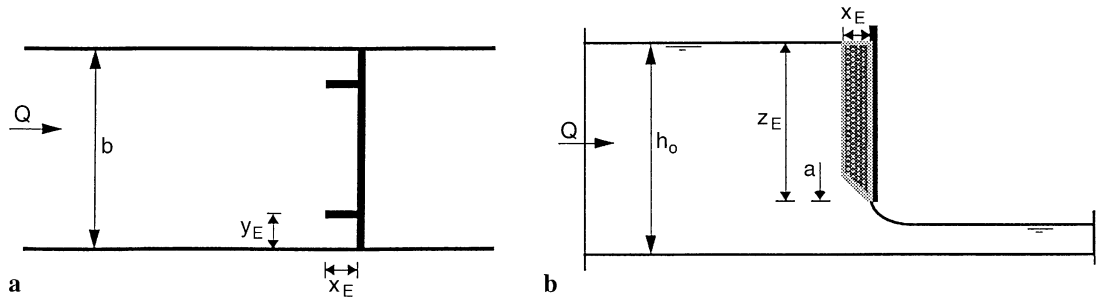




**Fig. 13a, b.** Anti-vortex element. **a** Plan, **b** side view

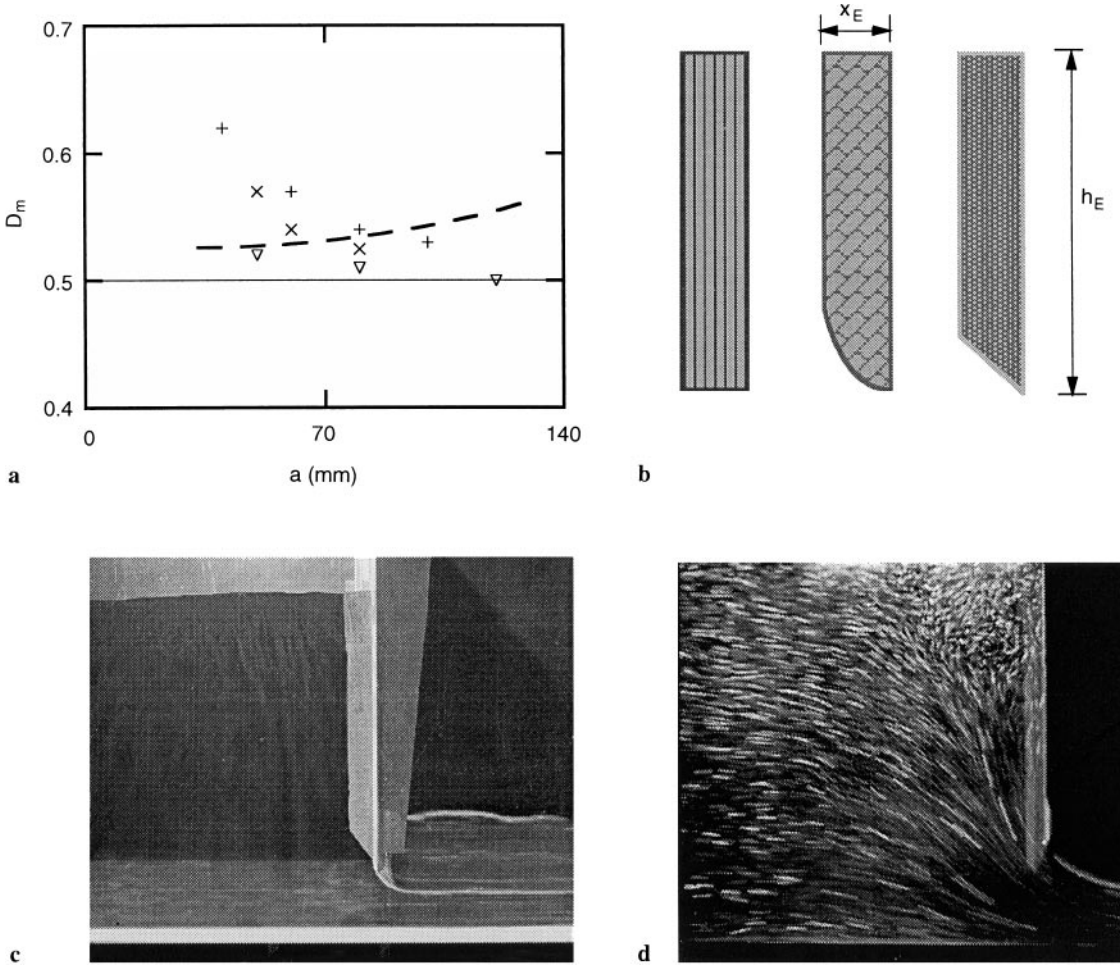


**Fig. 14a–d.** Anti-vortex element. **a** Reduction $D_m$ as a function of $a$(mm), (- - -) limit between flows with and without scale effects, **b** designs of anti-vortex elements, **c** gate flow with anti-vortex element mounted on front side, and resulting downstream flows at the front and rear channel sides, **d** corner vortices as origin of shock waves

## 5.3 Vortex intensities

Figure 12 refers to the intensities of intake vortices for the 500 mm wide channel as defined by Hecker (1984). For inviscid flows the vortex intensity is typically 5, and may vary from 4 to 6 provided $A > 0.15$. For $A < 0.15$, the intensity decreases sharply towards zero. For viscous flows ($a < 50$ mm) the vortex intensity is close to the gate opening $a$ in (cm). The vortex development thus varies strongly with both the relative gate opening $A$, and the absolute gate opening $a$.

## 6
## Anti-vortex element

### 6.1
### Optimisation procedure

The formation of shock waves downstream of gates is closely related to the generation of corner vortices upstream from the gate. Shock waves include the following disadvantages: (1) increase of required freeboard, (2) local air entrainment, and (3) asymmetry of tailwater flow. The following aims at a simple proposition to reduce significantly shock waves downstream of standard gates.

Two configurations to reduce shock waves have been tested: (1) vertical plates located close to the side walls to cut the transverse stagnation currents from the channel axis to the side walls, and (2) horizontal triangular plates located in the corners between the side walls and the gate to cut the vortex. The latter configuration was not effective, and was dropped. Figure 13 shows the so-called anti-vortex elements (subscript $E$) located upstream from the gate. These consist of two vertically mounted plates of length $x_E$ distant by $y_E$ from either channel wall of element height $z_E$. The optimization was made for $a = 50$ and 80 mm, and $b = 500$ mm. Criteria adopted were:

(1) reduction of shock waves,
(2) removal of corner vortices,
(3) simplicity and cost.

The lateral element position was optimum when it was located at the core of the vortex, i.e. $y_E = y_v$. Small deviations from this location were insignificant, particularly because the vortex is a highly dynamic phenomenon that is subject to temporal oscillation. The relative height $Z_E = z_E/(h_o - a)$ of the anti-vortex element was varied between 0 and 1, and its performance increased as $Z_E$ approached 1. The element must therefore be mounted over the entire height of the gate.

The relative length $X_E = x_E/y_v$ of the anti-vortex element was varied up to 2, and it was found that $X_E$ has no effect on the element performance for $X_E \geqslant 1$. However, the performance increased significantly as $X_E$ increased from 0 to 1, and $X_E = 1$ was the optimum element length. The element is thus characterized by $x_E = y_E = y_v$. The corner domain between the element and the wall has thus square shape in plan (Fig. 13a). The cross-sectional element geometry was varied as shown in Fig. 14b, including rectangular, slice-shape and triangular bottom shapes. No effect of geometry was evaluated, and the latter shape was selected because of ease in design.

### 6.2
### Shock wave reduction

The reduction of shock waves with the anti-vortex-elements positioned was determined with the parameter $D_m = (h_{rm} — h_u)/(h_s - h_u)$ where $h_{rm}$ = reduced shock wave height, $h_u$ = axial downstream flow depth, and $h_s$ = shock wave height without element (Fig. 1). Figure 14a shows data for both flows with and without scale effects (below dashed curve), and indicates a typical reduction $D_m = 50\%$. This reduction is significant, and the cost of installing anti-vortex elements is often much smaller than the disadvantages due to untreated downstream flow. The effect of the gate opening, $a$, on the shock wave reduction is small for flows without scale effects. The anti-vortex elements can easily be added to existing gates.

## 7
## Conclusions

Water flows under standard gates are subject to scale effects, depending on the absolute lengths of gate opening and channel width. For a gate opening below roughly 45 mm, viscous effects are always dominant, and the Froude similarity law ceases to apply. All additional results obtained in this study refer to inviscid flow, i.e. where scale effects are absent.



The position of ridge upstream from a gate depends exclusively on the relative gate opening and the capillary height. Both the velocity and pressure fields in the gate vicinity are analyzed and it was concluded that the effect of gate is confined to two gate openings upstream and downstream from the gate section. It is also demonstrated that the pressure force on a standard gate may significantly deviate from the pressure force based on hydrostatic pressure distribution.

The corner vortices upstream from a gate make gate flow a highly spatial phenomenon. Their effect on the shock waves downstream from the gate has been demonstrated. Also, the locations of the vortex center relative to the side wall and the gate have been determined, and the vortex intensities were defined. The shock waves can be significantly reduced with the so-called anti-vortex element. This novel device corresponds to a plate mounted on the gate with a 45° bevel at its lower crest. It is positioned into the center of the corner vortex and reduces the spatial flow pattern due to stagnation flow. The element can also be added to existing gates.

This project thus answers questions relating to a basic hydraulic device, for which the fundamental flow features have not been clarified yet. It aims also to introduce a simple device for significant shock wave reduction.

## References

**Boileau P** (1848) Mémoire sur le jaugeage des cours d'eau à faible ou à moyenne section. J Ecole Polytechnique Paris 33

**Bornemann KR** (1871) Versuche über den Ausfluss unter Wasser bei Schützen. Civilingenieur 17: 45–60

**Bornemann KR** (1880) Über den Ausfluss bei Schützen und schützenartigen Mündungen. Civilingenieur 26: 297–376

**Escande L** (1938) Etude théorique et expérimentale de l'écoulement par vanne de fond. Revue Générale de l'Hydraulique 4: 25–29; 4: 120–128

**Fawer C** (1937) Calcul de la contraction causée par une vanne plane dans le cas d'un écoulement dénoyé. Bulletin Technique de la Suisse Romande 63: 192–198; 63: 217–219; 63: 245–252; 63: 283–287

**Gentilini B** (1941) Efflusso dalle luci soggiacenti alle paratoie piane inclinate e a settore. L'Energia Elettrica 18: 361–380

**Gibson AH** (1920) Experiments on the coefficients of discharge under rectangular sluice-gates. Institution of Civil Engineers, Selected Paper 207: 427–434

**Haberstroh CE** (1890) Experiments on flow of water through large gates and over wide crests. J Assoc Eng Soc 5: 1–11

**Harber CD; Gulliver JS** (1992) Surface films in laboratory flumes. J Hydraulic Res 30: 801–815

**Hecker GE** (1984) Scale effects in modelling vortices. In: Proc. Symp. on Scale Effects in Modelling Hydraulic Structures, Technische Akademie Esslingen, ed. H. Kobus 6: 1–9

**Hurst HE; Watt DAF** (1925) The similarity of motion of water through sluices of the Assuan dam. Proc. Inst Civil Eng 218: 72–180

**Keutner C** (1932) Wasserabführungsvermögen von scharfkantigen und abgerundeten Planschützen. Bautechnik 10: 266–269; 10: 303–305
**Keutner C** (1935). Die Strömungsvorgänge an unterströmten Schütztafeln mit scharfen und abgerundeten Unterkanten. Wasserkraft und Wasserwirtschaft 30: 5–8; 30: 16–21
**Lewin J** (1995) Hydraulic gates and valves. Thomas Telford: London, UK
**Montes JS** (1997) Irrotational flow and real fluid effects under planar sluice gates. J Hydraulic Eng 123: 219–232
**Nago H** (1978) Influence of gate-shapes on discharge coefficients. Trans. Japanese Soc Civil Engr 10: 116–119

**Noutsopoulos GK; Fanariotis S** (1978) Discussion to Free flow immediately below sluice gates, by N. Rajaratnam. J Hydraulics Div ASCE 104: 451–454
**Rajaratnam N** (1977) Free flow immediately below sluice gates. J Hydraulics Div ASCE 103: 345–351; 103: 1371–1373; 104: 451–454; 104: 1462–1463
**Rajaratnam N; Humphries JA** (1982) Free flow upstream of vertical sluice gates. J Hydraulic Res 20: 427–436
**Rajaratnam N; Subramanya K** (1967) Flow equation for the sluice gate. J Irrigation Drainage Div ASCE 93: 167–168
**Smetana J** (1948) Ecoulement de l'eau au-dessous d'une vanne et forme rationelle de la surface d'appui de la vanne. La Houille Blanche 4: 126–146